Article

Air-stable van der Waals $PtTe_2$ conductors with high current-carrying capacity and strong spin-orbit interaction

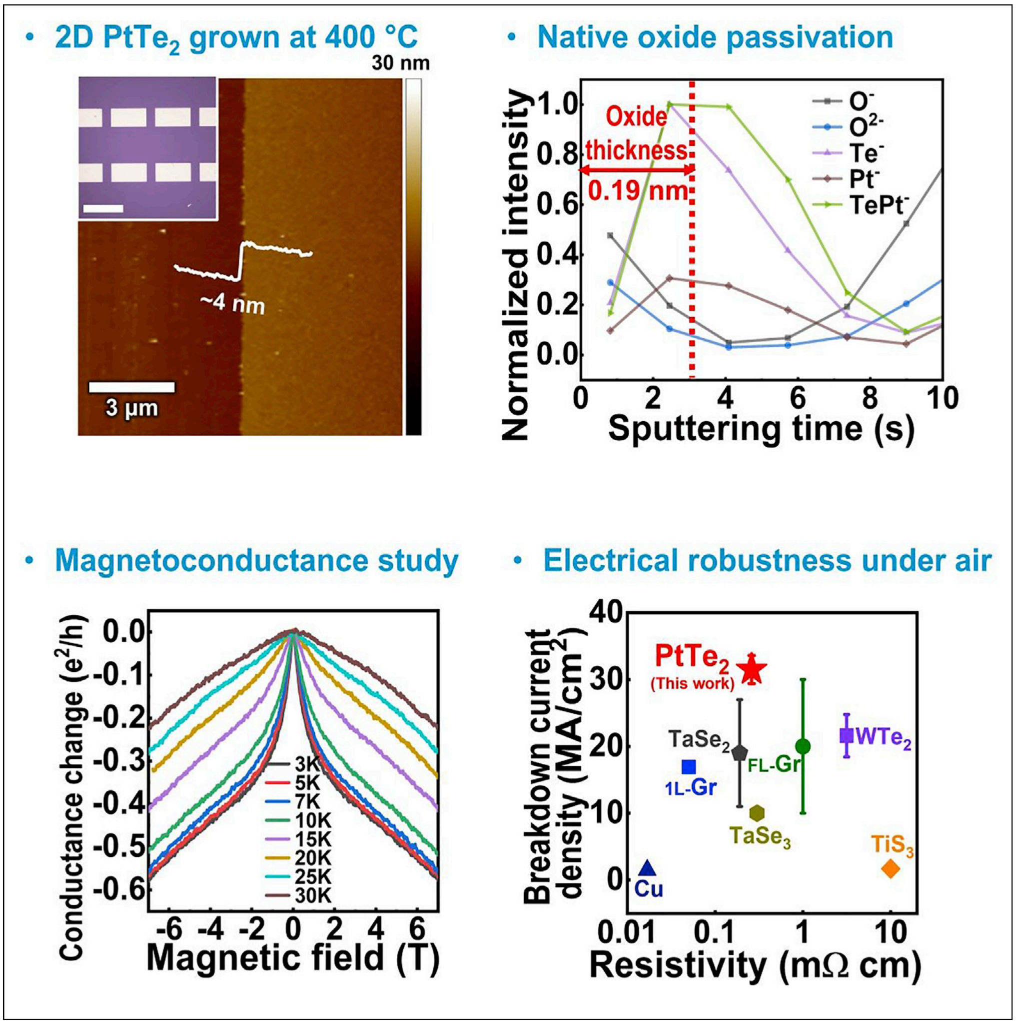

Seunguk Song, Inseon Oh, Sora Jang, ..., Zonghoon Lee, Jung-Woo Yoo, Soon-Yong Kwon

jwyoo@unist.ac.kr (J.-W.Y.)
sykwon@unist.ac.kr (S.-Y.K.)

Highlights

The synthesized $PtTe_2$ had a self-passivated surface under exposure to air

Magnetoconductance study proved the realization of a 2D confined quantum system

$PtTe_2$ sustained a remarkably high current density (~31.5 MA cm^{-2}) under air atmosphere

The native TeO_x passivation retarded the defect-induced electromigration of $PtTe_2$

Song et al., iScience *25*, 105346
November 18, 2022 © 2022 The Authors.
https://doi.org/10.1016/j.isci.2022.105346

iScience

CellPress
OPEN ACCESS

Article

Air-stable van der Waals $PtTe_2$ conductors with high current-carrying capacity and strong spin-orbit interaction

Seunguk Song,[1,3] Inseon Oh,[1,3] Sora Jang,[1] Aram Yoon,[1,2] Juwon Han,[1] Zonghoon Lee,[1,2] Jung-Woo Yoo,[1,*] and Soon-Yong Kwon[1,4,*]

SUMMARY

High-performance van der Waals (vdW) integrated electronics and spintronics require reliable current-carrying capacity. However, it is challenging to achieve high current density and air-stable performance using vdW metals owing to the fast electrical breakdown triggered by defects or oxidation. Here, we report that spin-orbit interacted synthetic $PtTe_2$ layers exhibit significant electrical reliability and robustness in ambient air. The 4-nm-thick $PtTe_2$ synthesized at a low temperature (∼400°C) shows intrinsic metallic transport behavior and a weak antilocalization effect attributed to the strong spin-orbit scattering. Remarkably, $PtTe_2$ sustains a high current density approaching $\approx$31.5 MA cm^{-2}, which is the highest value among electrical interconnect candidates under oxygen exposure. Electrical failure is caused by the Joule heating of $PtTe_2$ rather than defect-induced electromigration, which was achievable by the native TeO_x passivation. The high-quality growth of $PtTe_2$ and the investigation of its transport behaviors lay out essential foundations for the development of emerging vdW spin-orbitronics.

INTRODUCTION

In the past decade, there has been considerable advancement in two-dimensional (2D) van der Waals (vdW) materials, which have high potential to be used in next-generation electronics and spintronics because of their distinct physical and chemical characteristics (Song et al., 2020; Sung et al., 2017). Metallic transition-metal chalcogenides (TMCs) have recently attracted considerable attention because they show various quantum phenomena, such as topological phases (Amit et al., 2018), large magnetoresistance (MR) (Ali et al., 2014; Zhang et al., 2020), and charge density waves (Neal et al., 2014). Nevertheless, as it is difficult to synthesize TMCs with large areas and high quality, particularly vdW metallic tellurides (Song et al., 2020; Sung et al., 2017), new synthesis techniques are being extensively investigated. Most methods for synthesizing metallic TMCs (e.g., $TaSe_3$ (Empante et al., 2019), $ZrTe_3$ (Geremew et al., 2018), and WTe_2 (Song et al., 2019)) provide random small flakes on a substrate. Therefore, they are not scalable for conventional lithography techniques in on-chip applications. Furthermore, metallic TMCs are typically vulnerable to oxidation in ambient air (Lee et al., 2015; Pace et al., 2021; Stolyarov et al., 2016; Ye et al., 2016), which initiates the degradation of atomic structures within a few minutes, particularly for group-VI tellurides (Pace et al., 2021; Ye et al., 2016). Hence, it is highly desirable to fabricate a high-quality vdW metal in a 2D planar form and investigate its air stability for the versatile use of 2D metals.

$PtTe_2$ vdW crystal in a trigonal (1T) structure is an intriguing metallic TMC candidate because it has tilted topological surface states with spin-momentum locking, namely, type-II Dirac fermions (Amit et al., 2018). $PtTe_2$ provides high spin-charge conversion efficiency with strong spin-orbit coupling (SOC) and high electrical conductivity, which results in high spin-orbit torque (SOT) efficiency (Xu et al., 2020). Achieving a high current density of $PtTe_2$ (Ma et al., 2018a) can support the more effective generation of spin-transfer torque *via* the spin Hall effect, thereby providing a valuable platform for its use in spintronic devices. Furthermore, as it is essential to develop sharp and defect-free heterointerfaces for high-performance spintronics, metallic TMCs with vdW interfaces and efficient spin-charge conversion can be promising spintronic components to enhance spin injection instead of heavy 3D metals (e.g., Pt (Chen et al., 2021)) (Sierra et al., 2021; Zhang et al., 2021b). However, the spin-orbit scattering length of few-layered $PtTe_2$ has not

---

[1] Departmet of Materials Science and Engineering & Center for Future Semiconductor Technology (FUST), Ulsan National Institute of Science and Technology (UNIST), Ulsan 44919, Republic of Korea

[2] Center for Multidimensional Carbon Materials (CMCM), Institute for Basic Science (IBS), Ulsan 44919, Republic of Korea

[3] These authors contributed equally

[4] Lead contact

*Correspondence: jwyoo@unist.ac.kr (J.-W.Y.), sykwon@unist.ac.kr (S.-Y.K.)

https://doi.org/10.1016/j.isci.2022.105346

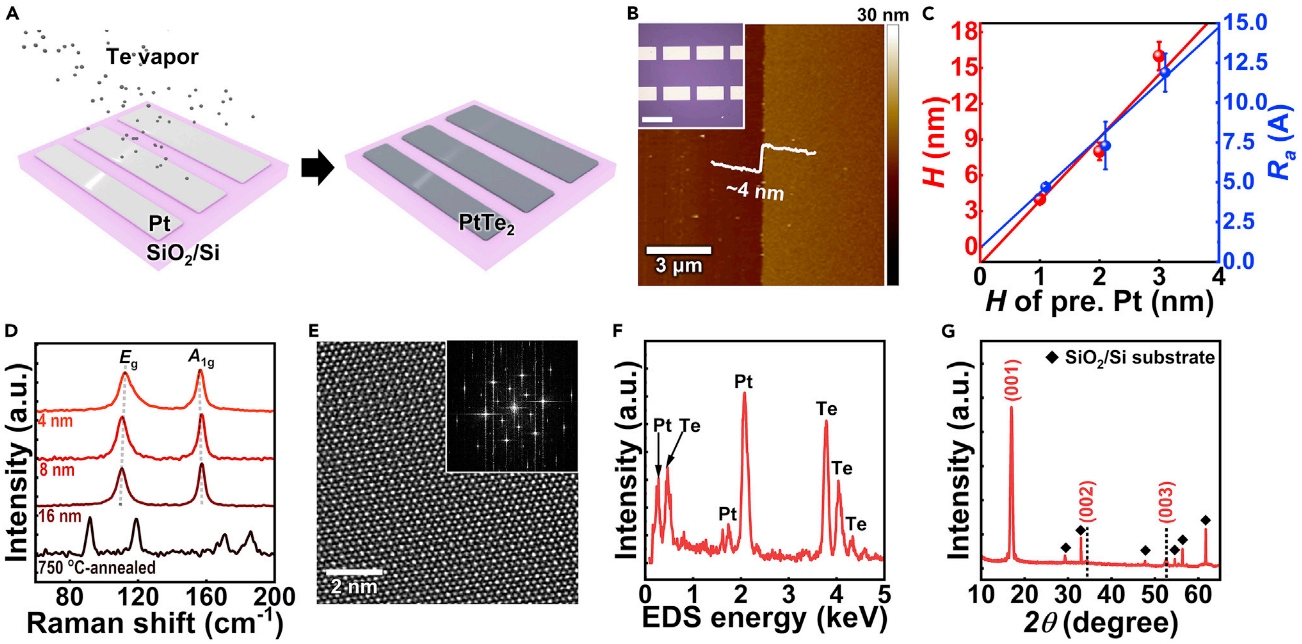

Figure 1. Position-controlled synthesis of vdW $PtTe_2$ thin films at CMOS-compatible low T

(A) Schematic of the growth of $PtTe_2$ layers on SiO_2/Si, where the powder-based vaporization of Te was conducted in a horizontal furnace at $T = 400°C$. The conformal $PtTe_2$ layers were created by tellurizing a Pt precursor patterned by conventional photolithography.

(B) Representative AFM image of an as-grown $PtTe_2$ film, showing a thickness (H) of ~4 nm. The inset shows the OM image of patterned $PtTe_2$ (scale bar: 200 μm).

(C) Summary of H and roughness (R_a) for $PtTe_2$ depending on H for pre-deposited Pt.

(D) Representative Raman spectrum of as-grown $PtTe_2$ thin films depending on H. Degraded $PtTe_{2-x}$ was obtained at $T = 750°C$.

(E) Atomic-resolution TEM image of the $PtTe_2$ thin film (inset: the corresponding fast Fourier transform patterns).

(F) TEM-EDS spectrum of the $PtTe_2$ thin film, showing the strong signals of Pt and Te with an almost perfect atomic ratio for $PtTe_2$ (at.% of (Te/Pt) ≈ 1.98).

(G) XRD pattern of $PtTe_2$ with distinguished (00l) peaks.

been investigated in detail, although it is necessary to understand carrier scattering and the SOC effect in conformally fabricated vdW thin films. Moreover, the high-field electrical transport and current-carrying capacity of $PtTe_2$ thin films (except irregular small flakes (Ma et al., 2018a)) have not been explored; these are crucial parameters for reliable operation and spin current generation in device applications.

In this study, we synthesize electronic-grade $PtTe_2$ thin films with controllable thickness and position at a complementary metal-oxide-semiconductor (CMOS)-compatible growth temperature of ~400°C. The 4-nm-thick $PtTe_2$ thin film exhibits intrinsic metallic transport without disorder-induced weak localization (WL) or the Kondo effect at low temperatures owing to the high-quality synthesis. A magnetoconductance study proves that 2D electron-electron interaction and weak antilocalization (WAL) occur in the presence of SOC, supporting the realization of a truly 2D confined quantum system. Furthermore, the $PtTe_2$ device can sustain a significantly high current density (~31.5 MA cm^{-2}) in ambient air, which is the highest value among air-exposed vdW TMCs until now. The result obtained using heat dissipation models suggests that the self-heating of the channel, rather than defect-induced electromigration, facilitates electrical robustness. Additionally, breakdown behaviors are similar regardless of the exposure of the device to air. Consequently, this study proposes the potential use of $PtTe_2$ in interconnects in integrated circuits or SOT devices with high reliability against oxidation-related degradation.

RESULTS AND DISCUSSION

Synthesis of $PtTe_2$ thin film with an ideal stoichiometry

The $PtTe_2$ thin film was produced using the powder-based tellurization of a Pt precursor (Figure 1A). The Pt precursor was deposited on the desired substrate (SiO_2/Si) located close to the Te powder at the center of a horizontal furnace. Then, it was heated to ~400°C under an H_2 atmosphere at a pressure of ~10 Torr. Vaporized Te formed an intermediate, i.e., H_2Te (heat of formation ≈ −146.4 kJ mol^{-1} (Zhou et al., 2017)), which reacted with the Pt precursor film while providing a relatively reactive environment compared to an Ar atmosphere. The low synthesis temperature (~400°C) allowed for the direct preparation of $PtTe_2$ on diverse substrates with minimal thermal degradation and compatibility with the CMOS technology. The microscopic morphology of $PtTe_2$ was determined by the photolithographic patterning of the pre-deposited Pt. This ensured the versatility of the position-controlled growth method. Atomic force microscopy (AFM) (Figure 1B) and optical microscopy (OM) (inset of Figure 1B) images indicated that the $PtTe_2$ thin film grown on SiO_2/Si had a uniform and flat surface. The thickness (H) of $PtTe_2$ linearly depended on the thickness of the Pt precursor owing to the volume expansion of Pt via tellurization (Figures 1C and S1). The 1-nm-thick Pt precursor was tellurized to form a $PtTe_2$ thin film with a uniform thickness of ~4 nm (roughness $R_a \approx 0.47 \pm 0.02$ nm). This was the thinnest film that was obtained, and it was used for most of the characterization in this study.

Raman spectroscopy showed the characteristic peaks of the crystal close to ~110 and ~157 cm^{-1}, which corresponded to the E_g and A_{1g} modes (Ma et al., 2018a), respectively (Figure 1D). This showed that $PtTe_2$ was successfully grown. The difference between the E_g and A_{1g} peaks increased with H ($\Delta \approx$ 44.3 and 47.2 cm^{-1} for $H \approx$ 4 and 16 nm, respectively). The Raman signals for non-stoichiometric $PtTe_{2-x}$ were absent for the as-grown thin film, whereas the film grown at 750°C showed the vibrational modes of PtTe (not $PtTe_2$) (Mc Manus et al., 2020; Zhang et al., 2021a) (the darkest spectrum in Figure 1D). As the vibrational mode of the PtTe crystal is frequently observed in the previous studies of synthesized few-layered $PtTe_2$ (Li et al., 2021; Ma et al., 2018a; Mc Manus et al., 2020; Zhang et al., 2021a), the lack of PtTe Raman peaks indicated the high crystallinity of the as-grown $PtTe_2$ film. In addition, Raman mapping was performed at four different areas (~$12 \times 12\ \mu m^2$) along the $PtTe_2$ film, which confirmed the film uniformity at the macroscopic scale (Figure S2). Figure S2B shows the Raman spectra captured at 1,600 different positions with a 300 nm interval, among which, one set was used for the Raman mapping (Figures S2C and S2D). The consistency in the peak positions and the intensity of E_g and A_{1g} modes indicate the spatial uniformity and high crystallinity of $PtTe_2$ across the measured area (~$12 \times 12\ \mu m^2$). Moreover, the Raman mapping images (Figures S2C and S2D) captured at positions 1–4 in the sample show comparable mapping contrasts.

Furthermore, transmission electron microscopy (TEM) analysis confirmed the high-quality growth of $PtTe_2$. The high-angle annular dark-field scanning TEM (STEM) image shown in Figure 1E demonstrated the distinctive hexagonal atomic arrangement of the 1T phase (Ma et al., 2018a) and lattice spacings of 0.20 and 0.35 nm for the (110) and (100) planes of $PtTe_2$, respectively. The TEM-energy-disperse spectroscopy (EDS; Figure 1F) and elemental mapping images of $PtTe_2$ (Figure S3) indicated almost ideal stoichiometry (at.% of (Te/Pt) ≈ 1.98) and the homogenous distribution of Pt and Te atoms. Furthermore, the cross-sectional STEM-EDS characterizations indicated the complete the tellurization of the Pt precursor and layer-by-layer growth of $PtTe_2$ (Figure S4). The layer-by-layer structure of $PtTe_2$ is clearly visible even near the $PtTe_2$/substrate interface in the HAADF-STEM image (near location A in Figure S4A). Furthermore, the EDS mapping images of Pt and Te show uniform distributions of the elements across the thin film (Figures S4B and S4C). The EDS spectra in Figure S4E show strong Te and Pt signals in the $PtTe_2$ film (Figure S4E). The EDS line profile of each element and the calculated atomic ratio between Te and Pt (at.% of (Te/Pt)) are presented in Figures S4F and S4G, respectively. The averaged at.% of Te/Pt was 1.75 ± 0.11 (mean ± standard deviation) without any evident stoichiometric change along the $PtTe_2$ thickness. The slight Te deficiency compared to its ideal stoichiometry (at.% of Te/Pt of 2.0) was caused by the FIB, which damaged the $PtTe_2$ during the cross-sectional sampling.

Moreover, the X-ray diffraction (XRD) pattern comprised the diffraction peaks of the (001L) planes of $PtTe_2$, indicating that the preferred orientation of the thin film in the direction normal to the substrate (Figure 1G). The XRD pattern did not exhibit any traces of Pt (111) or Pt (200) from the Pt precursor, which confirms the complete tellurization of Pt. We proposed that the uniform layer-by-layer growth of $PtTe_2$ through powder-based tellurization occurred because of the decreased flow rate of the carrier gas and low temperature. The slow reaction caused by the small Te flux prevented high nucleation densities (Kim et al., 2019) and/or the formation of a strained structure (Choudhary et al., 2018), which might have promoted the formation of vertically oriented 2D crystals at the initial growth stage (Choudhary et al., 2018; Wang et al., 2020). A high reactor pressure and high Te flux resulted in the aggregation of crystals and the production of micro-voids along the thin film (Figure S5).

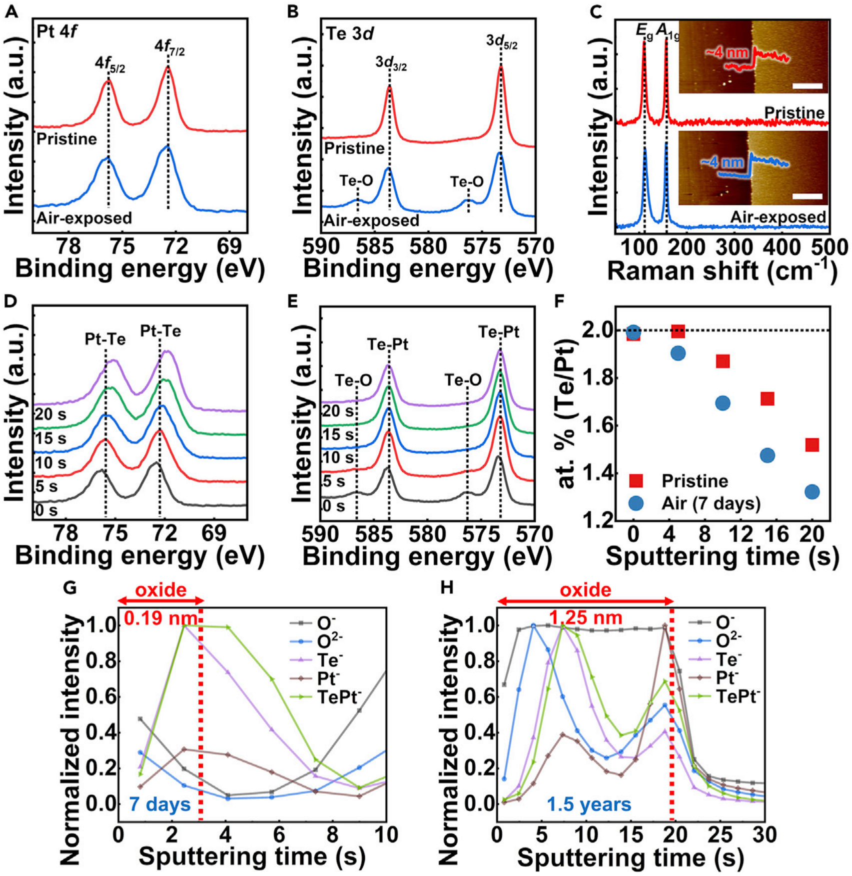

Figure 2. Surface property of $PtTe_2$ thin film under air exposure

(A and B) XPS spectra for the (A) Pt 4*f* and (B) Te 3*d* scans of $PtTe_2$, where the as-grown sample (red) and the sample exposed to air for seven days (blue) were characterized.

(C) Raman spectra of the $PtTe_2$ thin films with the different air exposure conditions (blue: the sample that was air exposed for seven days; red: as-grown sample). Inset shows the AFM images of the corresponding as-grown (top) and air-exposed (bottom) $PtTe_2$ thin films (scale bar: 1 μm). H and R_a did not change significantly after the air exposure.

(D–F) XPS analysis of air-exposed $PtTe_2$ with an Ar sputtering time of 0–20 s. (D and E) XPS spectra and (F) summary of the stoichiometry change depending on sputtering time. The dashed lines show the exact peak positions attributed to binding between Pt and Te in the as-grown sample from (A) and (B).

(G and H) Tof-SIMS depth profiles of $PtTe_2$ with different air exposure times, that is, (g) 7 days, and (H) 1.5 years, showing the intensities normalized to the maximum values of each emitted ion concentration. The vertical red dashed lines indicate the locations of the oxide layer formation, which were determined by comparing the concentrations of O^{2-} and O^- ions with those measured in the pristine $PtTe_2$ (Figure S5).

Self-passivated $PtTe_2$ surface under exposure to air

We examined the surface chemistry and oxidation behavior of as-grown $PtTe_2$ through X-ray photoelectron spectroscopy (XPS) (Figure 2A and 2B). The XPS spectra of as-grown $PtTe_2$ showed distinct peaks related to the chemical bonding between Pt and Te in the Pt 4*f* and Te 3*d* scans, and the measured peak intensities revealed the highly stoichiometric nature (at. % of (Te/Pt) ≈ 1.98) (red curves in Figures 2A and 2B). On the contrary, the sample exposed to ambient air at room temperature for 7 days showed an increase in Pt-Te ($4f_{5/2}$ and $4f_{7/2}$) and Te-Pt binding energies ($3d_{3/2}$ and $3d_{5/2}$) (blue curves in Figures 2A and 2B). The apparent oxidation features (Te-O binding) were observed at binding energies of ~576.3 and ~586.6 eV close to the Te-3*d*ays band (Figure 2B). In contrast, the core level for the Pt 4*d* scan in Figure 2A did not show extra peaks related to oxidation. The absence of Pt-O binding in the Pt 4*d* scan suggested that the main oxidation product of $PtTe_2$ was TeO_x, possibly because of oxidation at the top-most Te atomic layer. Furthermore, the calculated stoichiometry of air-exposed $PtTe_2$ was unaffected by oxidation (at.% of (Te/Pt) ≈ 1.98), indicating that most of the $PtTe_2$ structure was not degraded. This might have been because of the role of the native oxide as a passivation layer of TeO_x on the top most surface. In addition, the insignificant changes in the Raman spectroscopy (Figure 2C) and AFM images (insets of Figure 2C) depending on air exposure supported the negligible structural degradation. In addition, we performed XRD measurements of the as-grown $PtTe_2$ and that exposed to air for 7 days (Figure S6). The XRD patterns did not show a significant difference with respect to the (001*l*) peak positions and the full width at half maximum (FWHM), indicating that the XRD measurement could not detect the effect of oxidation on crystal quality. This oxidation behavior of $PtTe_2$ is considerably distinct from that of other vdW tellurides (WTe_2 (Ye et al., 2016) and $MoTe_2$ (Pace et al., 2021)), whose entire atomic structures are damaged within a few minutes of exposure to oxygen.

We quantitatively investigated the formation of TeO_x by performing XPS depth-profile characterization while etching the oxidized $PtTe_2$ (exposed to air ambient for 7 days) using the Ar ion bombardment technique (Figures 2D–2F). In the XPS spectra, the Te-O binding at ~576.3 and ~586.6 eV disappeared within 5 s of etching, and the peaks related to $PtTe_2$ shifted to lower energies (Figure 2E). The oxidized sample etched for 5 s showed a lack of Te (at.% of Te/Pt changed from 1.99 to 1.90 in Figure 2F), implying that Ar sputtering removed TeO_x instead of the atomic dissociation of O from the surface. In contrast, the as-grown sample sustained its ideal stoichiometry even after the initial sputtering for 5 s (red squares in Figures 2F and S7). The at.% of Te/Pt was maintained despite the change in the stoichiometry of oxidized $PtTe_2$ caused by the first sputtering. This suggested that the TeO_x structure caused relative structural vulnerability against the Ar etching. As further Ar sputtering was continued for more than 10 s, the at.% of (Te/Pt) decreased gradually because Ar sputtering typically results in preferential etching of chalcogen from a TMC crystal owing to its relative volatility (Baker et al., 1999). In addition, the rates of change in the atomic ratio (''at.% of Te/Pt'' per sputtering time) for pristine and air-exposed $PtTe_2$ became almost comparable because the structural instability of each sample became similar after the top-most Te or TeO_x layers were etched. The XPS peak of oxidized $PtTe_2$ shifted under sputtering for more than 10 s because of Te shortage (Figure 2D); this was also observed for pristine $PtTe_2$ (Figure S7). Consequently, we deduced that the oxidation of $PtTe_2$ preferentially occurred on the uppermost surface because the TeO_x passivation layer was created. On the contrary, negligible oxidation occurred on the underlying surface. The retarded oxidation by TeO_x may be beneficial for sustaining the intrinsic properties of $PtTe_2$ in air, as described in the following sections.

To investigate the oxidation behavior of $PtTe_2$, we performed time-of-flight secondary ion mass spectroscopy (ToF-SIMS) depth profile measurements for different $PtTe_2$ thin films depending on the duration of exposure to air, that is, 7 days and ~1.5 years (Figures 2G and 2H). A comparison of the depth profile of the pristine $PtTe_2$ film (Figures S8A and S8B) with that exposed for 7 days (Figures 2G and S8C) indicated that the major difference in O^- and O^{2-} concentrations occurred at the surface, which corresponds to the layer sputtered for 3 s. We estimated the thickness of this layer as ~0.19 nm, based on the measured etching rate of the film (~0.62 ± 0.01 Å/s up to 18 s sputtering). As the SIMS-extracted oxide thickness (~0.19 nm) was similar to the atomic radius of Te (~0.14 nm) or O (~0.15 nm), oxidation possibly occurred only in the top-most Te layers in $PtTe_2$ during its 1-week exposure to air. This is consistent with the results from the XPS characterizations of the air-exposed $PtTe_2$, which show a peak of TeO_x rather than PtO_x (Figures 2A and 2B). The negligible change in the thickness could not be detected via AFM at room temperature (Figure 2C), which further confirms the consistency of these results.

Moreover, the oxide layer thickness produced on the film via exposure to air for ~1.5 years was ~1.25 nm, because of the relatively high O^- and O^{2-} ion concentrations up to 20 s of sputtering in the ToF-SIMS depth profile (Figures 2H and S8D). The oxidation rate of the sample exposed to air for ~1.5 years was significantly low (~0.02 Å/day), and was 10 times smaller than that exposed for 7 days (~0.27 Å/day), suggesting that the surface passivation by oxide played a critical role in retarding further oxidation of the underlying $PtTe_2$. For the first 3 s of sputtering of $PtTe_2$ that was exposed to air for ~1.5 years (Figure 2H), the concentrations of O^- and O^{2-} were higher than those of Te^- or Pt^-; thus, the outermost surface of oxidized $PtTe_2$ was covered with oxygen up to the thickness of 0.19 nm, which is close to the atomic radius of O (~0.15 nm). Below the oxygen layer, the oxide penetrated the $PtTe_2$ bilayer (~1.06 nm) and formed a thin film.

We performed cross-section STEM imaging and spectroscopy analysis of the air-exposed $PtTe_2$ to investigate the produced oxides (Figures S4 and S9). However, it was impossible to accurately observe and distinguish the oxide structure produced by exposure to air via cross-sectional TEM because of the surface damage caused by the Ga ion beam during the focused ion beam (FIB) sampling used in the experiments

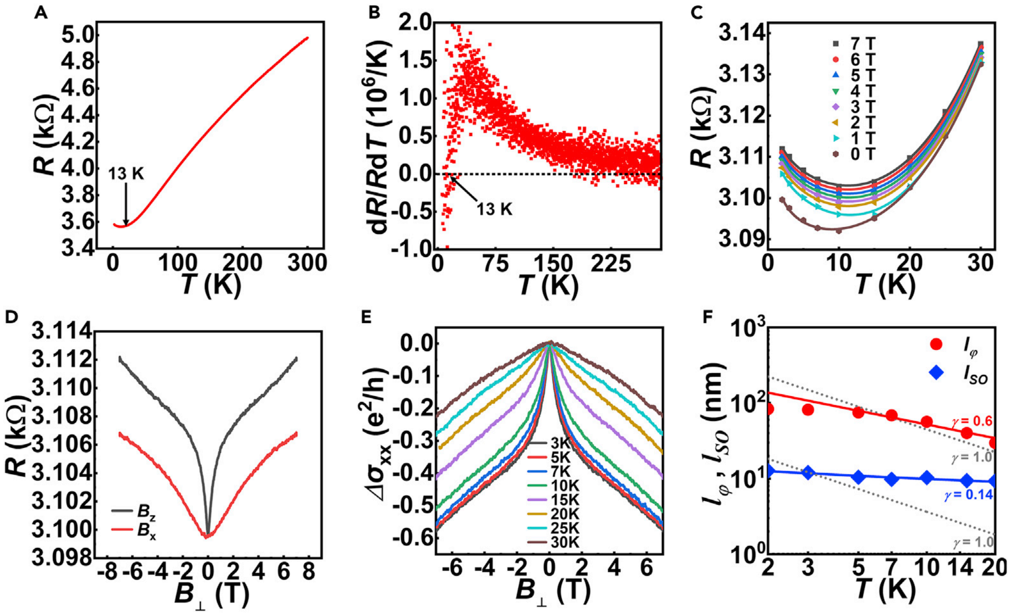

Figure 3. Low-temperature electrical transport of $PtTe_2$ under the applied magnetic field

(A) Four-probe resistance (*R*) vs. *T* plot showing a RRR (~1.39) for 4-nm-thick $PtTe_2$.

(B) Thermal resistance coefficient ($1/R \cdot dR/dT$) as a function of *T*, indicating the minimum value of *R* in (A) was obtained at around ~13 K.

(C) Temperature dependence of *R* measured at different magnetic fields ($0 < B < 7$ T), where *B* was applied perpendicular to the plane of the film. The data were fitted well to the expression for electron-electron scattering (Liu et al., 2019a).

(D) MR of $PtTe_2$ as a function of *B* at $T = 2$ K and $I_{ds} = 100$ mA. B_z and B_x indicate the magnetic field applied perpendicular to the plane of the film and parallel to the electrical field, respectively.

(E) Magnetoconductance ($\Delta\sigma_{xx}(B)$) measured at $T = 2$ K and $I_{ds} = 100$ mA displaying the WAL behavior.

(F) l_φ and l_{so} as a function of *T* extracted by using the HLN relation for WAL. Theoretical predictions suggest that dephasing from electron-electron interactions occurs at $l_\varphi = T^{-\gamma}$, where γ is 1.0 in 3D systems (indicated by the gray dashed curve for comparison) and γ is 0.5 in 2D systems (Hikami et al., 1980). The extracted l_φ in our $PtTe_2$ was fitted well to $l_\varphi = T^{-0.60}$ with an *R*-square value of 0.94 (red curve) and l_{SO} was almost independent of temperature (i.e., $l_{SO} = T^{-0.14}$) (blue symbols).

(See STAR methods section for detail). Nevertheless, no peaks corresponding to oxygen were observed in $PtTe_2$ under the FIB-damaged interface in electron energy loss spectroscopy (EELS) (Figure S9B) and EDS spectra (Figure S4E; labeled as C). This implies that the oxidation of $PtTe_2$ occurs layer by layer and gradually, which is consistent with that characterized via ToF-SIMS (Figures 2G and 2H).

Magnetoconductance of $PtTe_2$ with spin-orbit interaction

This section describes the low-temperature electrotransport and magnetotransport studies of as-grown 4-nm-thick $PtTe_2$ (Figure 3). Owing to the large-area and spatially controlled growth mode of $PtTe_2$, the transport study was conducted on a Hall bar device with a long channel length of ~1.7 mm fabricated using a conventional photolithography technique (Figure S10A). The temperature dependence (*R*–*T*) of the channel resistance shown in Figure 3A suggests a positive residual resistance ratio (RRR = R_{300K}/R_{2K}) of ~1.39 (at $T > 13$ K). This indicated the conducting mechanism of $PtTe_2$ is band transport as the temperature dependence of the conductivity of $PtTe_2$ exhibits metallic behavior without signatures of activations and/or hoppings. Hall measurement of the $PtTe_2$ thin film was performed at $T = 2$–30 K (Figures S10B and S10C). The Hall coefficient was positive (~2.0×10^{-10} $m^3A^{-1}s^{-1}$), indicating that most carriers in the material are holes in $PtTe_2$. The estimated carrier density (n_{3D}) and the Hall mobility (μ_{Hall}) were ~3.13×10^{22} cm^{-3} and ~2.06 $cm^2V^{-1}s^{-1}$ at $T = 2$ K, respectively. We compared the extracted n_{3D} and μ_{Hall} values with those in previous reports on $PtTe_2$ in Table S1. The μ_{Hall} of as-synthesized $PtTe_2$ was higher than those reported for chemically synthesized $PtTe_2$ with similar thicknesses (Hao et al., 2018; Ma et al., 2018a), indicating the high quality of our $PtTe_2$ crystal. Although the grain boundaries (GBs) of polycrystalline $PtTe_2$ can reduce its electrical mobility by the GB scattering mechanism (Ma et al., 2017), the comparable μ_{Hall} of our $PtTe_2$ (~2.06 $cm^2V^{-1}s^{-1}$) to those of CVD-grown single crystal (~0.46–1.06 $cm^2V^{-1}s^{-1}$) (Ma et al., 2018a) demonstrated the GB scattering effect was minor in our polycrystalline $PtTe_2$ thin film. The negligible GB scattering effect might be attributed to the more than 10 times wider grain size (~30–50 nm in Figure S3) than its thickness of $PtTe_2$ (~4 nm), which results in the almost negligible increase (<10%) in the resistivity by GB scattering (Adelmann et al., 2014; Gall, 2020; Steinhögl et al., 2002; Zhou and Gall, 2018).

In Figure 3B, a negative dR/dT was observed below 13 K, which could be attributed to the defect-induced Kondo effect, WL, or electron-electron scattering (Liu et al., 2019a, 2019b). We validated the exact transport mechanism at $T < 13$ K by investigating the R-T behavior for different magnetic fields ($0 < B < 7$ T) applied perpendicular to the plane of the film (I_{ds}) (Figure 3C). The negative dR/dT (i.e., resistivity upturn in Figure 3C) was not suppressed by the magnetic field; this suggested that the Kondo effect and WL did not occur (Liu et al., 2019b). Instead, electron-electron scattering occurred in the high-quality crystal (Liu et al., 2019a), as expected, and it fitted well (R-square > 0.99) to the curves shown in Figure 3C, as follows (Liu et al., 2019b):

$$\rho(T) = \rho_0 + BT^3 - Cln(T) - DT^{\frac{1}{2}} \qquad \text{(Equation 1)}$$

where ρ_0 is the residual resistance, B is the parameter contributed by electron-phonon scattering, and C and D are attributed to 2D and 3D electron-electron interactions, respectively. C (~5.83) was larger than B (~0.002) and D (~0.92) (Figure S10D). This implied nontrivial quantum interference effect resulted from 2D electron-electron interactions in the high-quality $PtTe_2$ thin film rather than 3D transport or disorder-induced scattering.

Figure 3D shows the MR of the $PtTe_2$ thin film. Under a strong magnetic field (>7 T), the MR linearly increased with B. The MR reached ~0.4% and ~0.2% for the magnetic fields that were perpendicular to the plane of the film (B_z) and parallel (B_x) to the I_{ds} direction, respectively. The linear and anisotropic MR was similar to that of a bulk $PtTe_2$ single crystal with a tilted Dirac dispersion (Amit et al., 2018). This indicated that a similar band structure was maintained for the patterned $PtTe_2$ with a thickness of ~4 nm. A strong WAL signal was observed, which was indicated by the shape of the cusp under a weak magnetic field (<2 T). This WAL could be induced by the elastic scattering of carriers in the presence of SOC.

We further examined the WAL behavior of the magnetoconductance measured at various temperatures ($3 < T < 30$ K; Figures 3E and S10E–S10G) by fitting to the Hikami, Larkin, and Nagaoka (HLN) theory for a 2D single-band system in the presence of SOC (Hikami et al., 1980):

$$\Delta\sigma(B) = \sigma_{xx}(B) - \sigma_{xx}(o) = -\frac{e^2}{\pi h}\left[\frac{1}{2}\psi\left(\frac{1}{2}+\frac{B_\varphi}{B}\right) - \frac{1}{2}\ln\left(\frac{B_\varphi}{B}\right) - \psi\left(\frac{1}{2}+\frac{B_\varphi+B_{SO}}{B}\right) + \ln\left(\frac{B_\varphi+B_{SO}}{B}\right) - \frac{1}{2}\psi\left(\frac{1}{2}+\frac{B_\varphi+2B_{SO}}{B}\right) + \frac{1}{2}\ln\left(\frac{B_\varphi+2B_{SO}}{B}\right)\right] \qquad \text{(Equation 2)}$$

Here, $B_\varphi = \frac{\hbar}{4De\tau_\varphi} = \frac{\hbar}{4el_\varphi^2}$, $B_{SO} = \frac{\hbar}{4De\tau_{SO}} = \frac{\hbar}{4el_{SO}^2}$, $\psi(x)$ is the digamma function, B_φ is the dephasing magnetic field determined by the phase coherence time (τ_φ) or phase coherence length (l_φ), and B_{SO} is the spin-orbit scattering field determined by the spin-orbit scattering time (τ_{SO}) or spin-orbit scattering length (l_{SO}). Our results also fit well with the reduced HLN expression (shown in Figure S10F), suggesting a dominance of the 2D scattering mechanism. The temperature dependence of l_φ and l_{SO} was investigated within a power law (Hao et al., 2018): $l \propto T^{-\gamma}$ (Figure 3F). The fitted γ values for l_φ was ~0.60, which was comparable to the ideal value of ~0.5 for the dephasing induced by 2D Nyquist electron-electron scattering, and the l_{SO} was nearly independent of temperature (i.e., $l_{SO} = T^{-0.14}$). As l_φ was larger than l_{SO} ($\tau_{SO}/\tau_\varphi < 1$), spin-orbit scattering occurred in phase-coherent transport, which resulted in positive MR and WAL in the 2D system (Liu et al., 2019a; Zhang et al., 2020). The dephasing length ($l_\varphi \approx 83.5$ nm at $T = 2$ K) was much larger than the thickness (~4 nm) of $PtTe_2$ at the T regime of 2–20 K, suggesting that the transport occurred in the truly 2D quantum diffusion system (Altshuler et al., 1982; Zhang et al., 2020). The extracted l_φ (~83.5 nm) was larger than the coherence length of 2D TMDs with large atomic numbers (~40 nm at 2 K in WTe_2 (Naylor et al., 2017), ~50 nm at 1.9 K in VSe_2 (Liu et al., 2019a), and ~50 nm at 400 mK in MoS_2 (Neal et al., 2013)). However, l_{SO} (~12.7 nm) was comparable to the spin diffusion length of Pt (~12 nm) (Niimi et al., 2013), which is widely used in the calculation of the spin Hall effect. This result indicates that the synthesized vdW $PtTe_2$ thin film is a promising candidate for application in future spin-orbitronic devices with strong SOC.

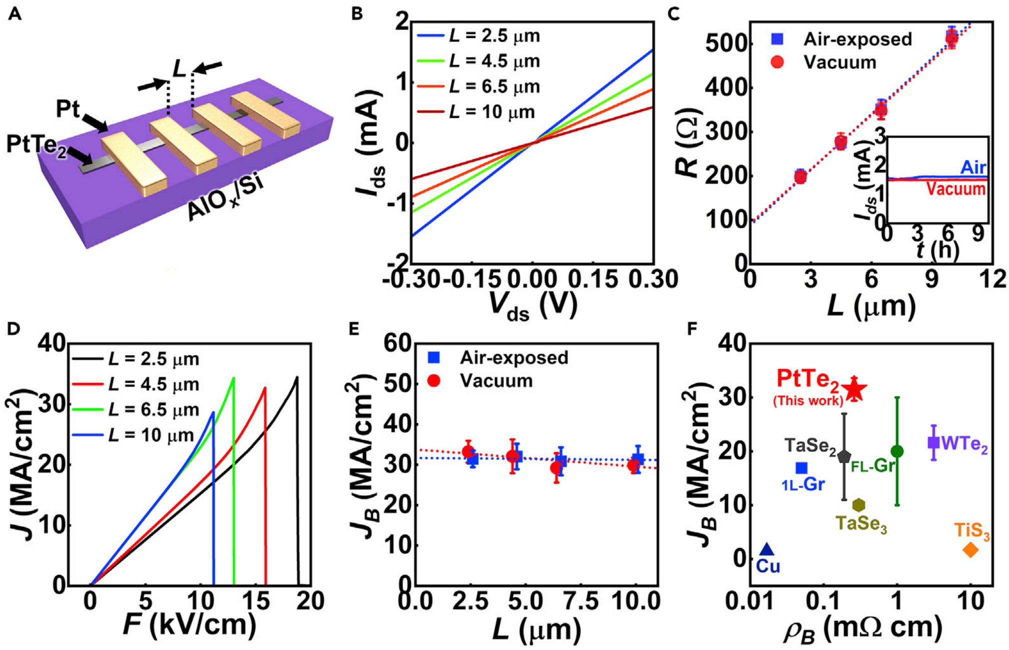

Figure 4. Electrical characterization of PtTe$_2$ in vacuum and ambient air at room temperature

(A) Schematic of the PtTe$_2$ device with Pt contact electrodes consisting of TLM patterns with different channel lengths (L).

(B) Representative two-probe I_{ds}-V_{ds} plot of PtTe$_2$ ($H \approx 4$ nm). The channel width (W) was ~18.4 μm (Figure S7).

(C) TLM plots for the corresponding PtTe$_2$ devices, measured in air (blue) and vacuum (red). The six sets of TLM devices were averaged, and the error bars indicate each standard deviation. The same linear fits for the plot measured under each condition demonstrate considerably similar values of R_s and R_c. (inset: constantly measured I_{ds} depending on t, without any decrease in I_{ds} under air exposure. V_{ds} = ~0.3 V was applied during the measurement, which corresponded to a current density (J) of ~2 MA/cm^2.

(D–F) Electrical breakdown investigation of the PtTe$_2$ devices under a high-bias field (F). (D) Representative J-F plot for the devices with different values of L measured under vacuum. The abrupt decrease in J was attributed to the device breakdown caused by the high-bias stress, where the maximum value of J corresponded to the breakdown current density (J_B). (E) The average value of J_B depending on L in air and vacuum. The dashed linear fit is shown as a visual guide. (F) Benchmark plot for J_B and ρ_B measured in air. PtTe$_2$ showed the highest value of J_B and a low value of ρ_B compared to other materials such as graphene (few-layer (FL-Gr) (Lee et al., 2011) and monolayer (1L-Gr) (Kang et al., 2011)), TMCs (TaSe$_2$ (Neal et al., 2014), TaSe$_3$ (Stolyarov et al., 2016), TiS$_3$ (Molina-Mendoza et al., 2017), and WTe$_2$ (Song et al., 2019)), and conventional interconnect materials (Cu (Rathmell and Wiley, 2011)).

Electrical breakdown of PtTe$_2$ under high bias

We evaluated the electrical reliability of PtTe$_2$ under a wide range of bias conditions, which should be considered for its potential application in spin-transfer torque devices. We facilely fabricated the devices using a transfer-length method (TLM) by depositing Pt contact electrodes (~40 nm) on the spatially aligned PtTe$_2$ line patterns with a width (W) of ~18.4 μm and H = ~4 nm (Figure 4A, S11A, and S11B). For a systematic characterization under vacuum and air exposure, we fabricated two groups of on-chip devices by simultaneously growing and fabricating PtTe$_2$ devices (see STAR methods for more details). A linear I_{ds}-V_{ds} plot was obtained under a low bias ($V_{ds} < 0.3$ V), indicating the realization of an ohmic contact (Figures 4B and S11C). The current varied with the channel length (L). This allowed for the extraction of the sheet resistance (R_s) and contact resistance (R_c) of PtTe$_2$ from the TLM plot (Figure 4B). The PtTe$_2$ layers under vacuum exhibited R_s = ~765 ± 36 Ω/sq (≈0.37 ± 0.01 mΩ cm) and R_c = ~0.85 ± 0.08 mΩ cm, which were measured in at least six different TLM groups. Furthermore, there were minor variations (~4–9%) among the TLM devices.

We conducted the same electrical measurement in ambient air to investigate the carrier transport during oxidation for different TLM device sets fabricated on another chip. Notably, R_s and R_c values were almost unchanged under air exposure; for example, R_s = 779 ± 20 Ω/sq and R_c = 0.81 ± 0.03 mΩ cm were obtained under air exposure (Figures S11D and S11E). Because the Pt contact electrodes were already deposited on top of $PtTe_2$ prior to air exposure, the oxidation of $PtTe_2$ beneath the electrode-contacted area was further delayed, resulting in a minor change in interfacial R_c (~4.7% in Figures S11D and S11E). Even under electrical stress in air, two-terminal I_{ds} at a constant bias of 0.3 V did not noticeably degrade with the measurement time (t) of ~10 h, as shown in the inset of Figures 4C and S11F. However, it showed a slight I_{ds} increase (~3.9%), which may be attributed to the *p*-type doping by the absorbed oxygen molecules (Liang et al., 2020). Because the major carriers of $PtTe_2$ are holes, as characterized by Hall measurements in Figure S10B, the conductivity increases owing to the charge transfer between the absorbed oxygen and $PtTe_2$. Moreover, the migration of oxygen ions along the oxidized surface triggers conductivity variation, which is similar to the behavior observed in the endurance test for oxide-based resistive memory devices (Kim et al., 2010). Nevertheless, the insignificant change in I_{ds} (~3.9%) in an oxygen-rich atmosphere is typically not expected for nanomaterials (e.g., Cu nanowires (Rathmell and Wiley, 2011), MXene (Lipatov et al., 2016), WTe_2 (Song et al., 2019), and phosphorene (Island et al., 2015)), implying the considerably high air stability of $PtTe_2$. Based on the XPS results of air-exposed $PtTe_2$ (Figure 2), the electrical properties of $PtTe_2$ may be attributed to the passivation layer of TeO_x on the surface.

In addition to the low-field electrical study, high-bias characterization showed the electrical robustness of surface-oxidized $PtTe_2$ (Figures 4D–4F). Figure 4D shows the typical current density (J) *vs.* electrical field (F) curves for $PtTe_2$ with different values of L. The curves were obtained up to the electrical breakdown, where J decreased abruptly. The maximum breakdown current density (J_B) approached ~44 MA/cm^2 at 30 K and ~38.6 MA/cm^2 at 298 K for the devices with $L = 2.5\ \mu m$ under vacuum (Figures 4D and S12). These values were almost two orders of magnitude higher than those of conventional interconnect metals (~several MA/cm^2) (Rathmell and Wiley, 2011). Remarkably, J_B measured under air exposure (31.5 ± 2.1 MA/cm^2 on average) was almost the same as the pristine current-carrying capacity, as depicted in Figure 4E (and Figures S13A and S13B). This implied that the air stability of $PtTe_2$ was maintained even under high-bias tests. It is worth noting that the averaged J_B in air (~31.5 ± 2.1 MA/cm^2) for $PtTe_2$ is the highest reported value among vdW metals (e.g., Graphene (Kang et al., 2011; Lee et al., 2011), $TaSe_2$ (Neal et al., 2014), $TaSe_3$ (Stolyarov et al., 2016), WTe_2 (Song et al., 2019), and TiS_3 (Molina-Mendoza et al., 2017)) and 3D conventional interconnect materials (e.g., Cu (Rathmell and Wiley, 2011)) in an oxygen-rich atmosphere (Figures 4F and Table S2). Combined with the comparatively low resistivity ($\rho \approx 0.26\ m\Omega$ cm), the high value of J_B indicates that $PtTe_2$ can be used as an on-chip conducting element in air. Furthermore, the high current-carrying capacity of $PtTe_2$ with the spin-orbit interaction (Figure 3) suggests its potential for use in vdW spin-torque devices. For example, SOT-driven magnetic random memory requires a high current density of 20–40 MA/cm^2 during its writing process (Fukami et al., 2016; Shi et al., 2018); therefore, 2D $PtTe_2$ can be used as a reliable conducting element in 2D integrated SOT devices.

Investigation of electrical breakdown mechanism

We further analyzed the electrical breakdown mechanism using scanning electron microscopy (SEM) and EDS analysis of the $PtTe_2$ devices after electrical stress in air (Figures 5A–5C). The different contrast in the SEM image of the $PtTe_2$ channel represented the breakdown location (Figure 5A, left), which was indicated by the darker contrast caused by the backscattered electron (BSE) mode (i.e., BSE signal $\propto$ atomic number, Z) (Figure 5A, right). The SEM-EDS spectra were confocally obtained close to the micro-voids, and they are shown in Figure 5B. Te (black) element was not detected at the micro-voids, in contrast to the areas at a distance from the micro-voids (red). This implied that the atomic displacement was more severe for Te compared to Pt. The absence of Te suggested that its electrical breakdown occurred owing to the atomic evaporation of Te via self-heating, as a high electrical field can typically induce the instability of chalcogen atoms in TMCs (Song et al., 2019; Stolyarov et al., 2016). Particularly, the electrical breakdown of $PtTe_2$ can be a result of the applied forces; i.e., (i) self-heating effects and (ii) electron wind force, as depicted in Figure S13C. These processes may take place almost simultaneously during the electrical failure while affecting each other. Since the heat generated at the center of the device and transported underneath heat sink and electrodes, the failure possibly located at the middle point of the $PtTe_2$ channel if the breakdown is solely relies on Joule heating. This implies that fast heat dissipation through the contacted interface/substrate is important to sustain high current density in $PtTe_2$. On the other hand, momentum transfer by electron-wind force (F_{wd}) can dominate the electrical failure, which results in the atomic flux appearing between the cathode and anode driven by F_{wd}, leaving behind voids near the cathode close to the self-heated region, but not at the exact center of the channel. Both elevated diffusivity (D) by thermal effect and high F_{wd} results in electromigration, which breaks the Pt-Te bond at the lattice and transport atoms (J_{atom}) to anode leaving behind vacancies ($J_{vacancies}$) (Nguyen et al., 2004) if an electrical breakdown is

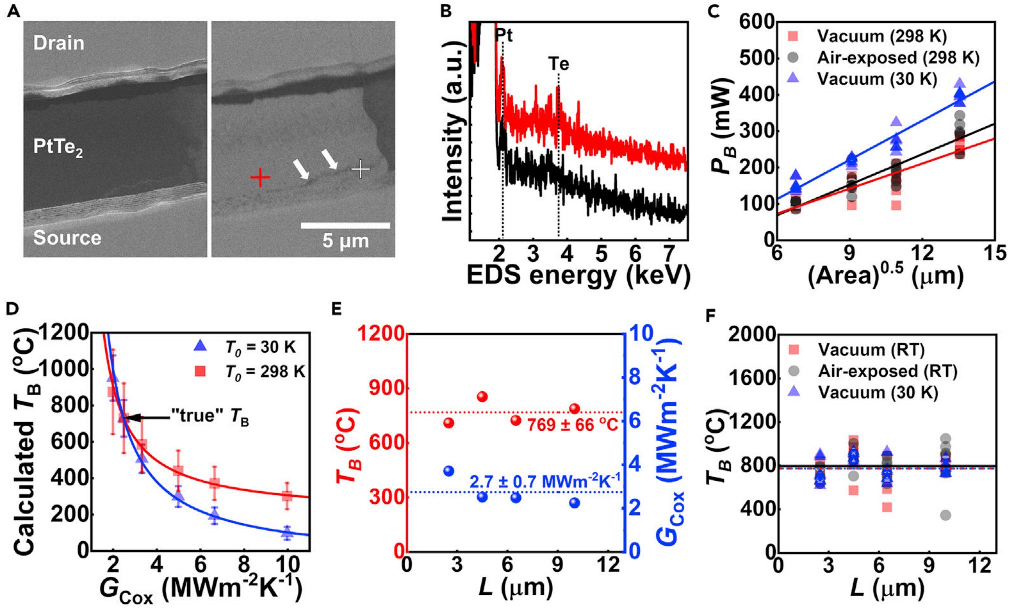

Figure 5. Investigation of electrical breakdown mechanism

(A) SEM images of a representative device obtained in the SE (left) and BSE modes (right). The SEM images were obtained after the electrical breakdown of the device in air. As Pt and Te are relatively heavy atoms, $PtTe_2$ showed a brighter contrast compared to other elements, allowing for the identification of failure locations in the BSE-SEM image (indicated by white arrows).

(B) SEM-EDS spectra measured for the remaining $PtTe_2$ channel under high bias, marked as red and black crosses in (a), respectively.

(C–F) Self-heating-induced electrical failure investigated using the thermal dissipation model. (C) Applied electrical power up to failure (P_B) *vs.* channel area in contact with the substrate ($(WL)^{0.5}$) measured under different conditions (vacuum and air) and values of T_0 (30 and 298 K). The data were fitted well to the heat dissipation model (linear lines). (D) Dependence of the calculated Joule-heating-induced breakdown temperatures (T_B) on the thermal boundary conductance between $PtTe_2$ and oxide layers (G_{Cox}) at different ambient temperatures (T_0) for L = 2,500 μm. The curves were fitted to the heat dissipation law as a function of G_{Cox}. As T_B is an intrinsic property of a material (does not depend on T_0), we extracted the "true" values of T_B and G_{Cox} at the intersection point of the two modeled curves. (E) Summary of T_B and G_{Cox} characterized under vacuum depending on L. The average value of T_B was ~769 ± 66°C, and G_{Cox} was ~2.7 ± 0.7 $MWm^{-2}K^{-1}$. (F) Comparison of T_B for each device under different ambient conditions and values of T_0. The colored dashed lines show the average value of T_B for each condition; these values are similar.

mainly caused by electromigration. In our experiments for 26 devices, we found that the failure locations were rather near the center of the channel (~48.9 ± 25.5%), not at the contacts (0 or 100%), as displayed in Figure S13D. This indicates that the behavior was not dominantly dependent on the F_{wd}. We suppose that the Joule heating-related electrical breakdown happens primarily since the synthetic $PtTe_2$ did not have severe defects to trigger defect-induced electromigration.

The ambient temperature of the measurement (T_0) affected the maximum input power up to failure (P_B). For instance, the average value of P_B was 167.3 ± 66.0 mW at room temperature. It increased to 262.3 ± 98.6 mW as T_0 decreased to ~30 K (Figure 5C) because a lower value of T_0 increased Joule heating until material breakdown. Furthermore, P_B increased linearly with the contact area of the substrate ($WL^{0.5}$). This indicated that the electrical breakdown behavior followed the trend of self-heating, expressed as the following heat dissipation model (Liao et al., 2010; Mleczko et al., 2016; Song et al., 2019):

$$P_B \approx g(T_B - T_0)L \qquad \text{(Equation 3)}$$

Here, T_B is the maximum temperature affected by Joule heating at the breakdown and g is the interfacial thermal conductance of $PtTe_2$, which is the parallel combination of the thermal resistance of the oxide (R_{ox}), the thermal resistance from the oxide to Si (R_{si}), and the thermal contact resistance between the channel and oxide interface (R_{Cox}). g was proportional to $(W/L)^{1/2}$ for the dimensional constraints of $PtTe_2$

(Figure S14), indicating a well-fitted self-heating model for our data (see STAR methods sections for details on the heat dissipation model). Note that the lateral heat dissipation from $PtTe_2$ to the Pt contact electrodes is not included in the above thermal model because the thermal healing length ($L_H \approx 45$–100 nm) is significantly smaller than the channel length (~2.5–10 μm); hence, its contribution is negligible (Figures S9B and S9C).

The value of P_B measured in air ($\approx 183.4 \pm 75.3$ mW) was analogous to that in vacuum ($\approx 167.3 \pm 66.0$ mW) in Figure 5C, indicating that the oxidation of $PtTe_2$ did not alter the reachable value of T_B or the electrical failure mechanism. We estimated an appropriate value of g to extract T_B using Equation 3 (Figures 5D–5F). In principle, g was estimated by arbitrarily assuming G_{Cox} ($1/R_{Cox}$) in the range of ~1–10 $MWm^{-2}K^{-1}$ and using the dependence of R_{ox} (Cappella et al., 2013) and R_{si} (Song et al., 2019) on T. This allowed for the extraction of T_B by applying Equation 3 to the value of P_B obtained at different values of T_0 (see details in STAR methods sections)Figure S14. Figure 5D shows the values of T_B obtained for different values of G_{Cox} at T_0 = ~30 and ~298 K using the data for the $PtTe_2$ devices with L = 2,500 μm in a vacuum. As T_B is an intrinsic material property (not affected by T_0), the intersection point of the two different curves fitted to the reduced heat dissipation model denoted the "true" values of T_B and R_{Cox}. The $PtTe_2$ devices in vacuum showed similar values of T_B and G_{Cox} regardless of L (Figure 5E). The average value of T_B was 769 ± 66°C, and G_{Cox} was 2.7 ± 0.7 $MWm^{-2}K^{-1}$. G_{Cox} was similar to those for the interfaces between vdW materials and oxides (Table S3), indicating the accuracy of our inference using a heat-dissipation model. T_B = ~750–825°C corresponded to the temperature at which the destructive loss of Te started on the surface of $PtTe_2$ (~750°C) (Mc Manus et al., 2020); this supported our hypothesis of self-heating-induced electrical breakdown.

For G_{Cox} = ~2.7 $MWm^{-2}K^{-1}$, the average value of T_B for air-exposed $PtTe_2$ with different values of L was calculated to be ~797 ± 152°C (Figure 5F). The similar values of T_B obtained under different conditions suggested that ambient air had a negligible effect on thermal degradation. This phenomenon is different from other vdW metals; for example, self-heating by high bias typically accelerates oxidation at defect sites (Kang et al., 2011; Song et al., 2019), resulting in smaller values of T_B, $P_{B,}$ and consequently J_B in air. We propose that the high quality of our synthetic film without impurities can prevent fast atomic displacements triggered by defects. Moreover, as the oxide layer partially formed at the top-most surface of $PtTe_2$ (Figure 2), further oxidation could be retarded to obtain a high current-carrying capacity in an oxygen-rich atmosphere. Therefore, the use of self-passivated high-quality $PtTe_2$ may provide highly reliable performance for vdW-integrated devices for electronics and spintronics under high bias.

Conclusions

We studied the air-stable electrical-transport behavior of a vdW $PtTe_2$ thin film with spin-orbit interaction. We introduced the position-controlled and thickness-controlled growth of a high-quality $PtTe_2$ thin film at a centimeter scale, demonstrating a highly stoichiometric nature and high electrical conductivity. The XPS study and ToF-SIMS depth profile of air-exposed $PtTe_2$ showed that the binding between Pt and Te was sustained even under surface oxidation for 7 days, which was attributed to delayed oxidation of layer by the top-most TeO_x passivation. Low-temperature electrotransport and magnetotransport studies of $PtTe_2$ revealed the quantum interference effect caused by 2D electron-electron interaction and the short spin-orbit scattering length ($l_{so} \approx 12.7$ nm), which was comparable to that of Pt. This may be extensively utilized for the effective spin-charge conversion in various vdW spin-orbitronic devices. Furthermore, $PtTe_2$ showed a high current-carrying capacity regardless of exposure to air. J_B was ~31.5 MA/cm^2 under air at room temperature and ~44 MA/cm^2 at 30 K under vacuum. The electrical breakdown followed the ideal pattern of heat dissipation, which indicated that the primary failure mechanism was the self-heating of $PtTe_2$ of up to ~750°C rather than defect-induced electromigration.

Our study demonstrates the reliability and versatility of vdW $PtTe_2$ conductors for use in next-generation electronic and spintronic applications. For example, developing a novel and reliable 2D conductor compatible with a 2D semiconductor is critical considering the requirements of the semiconductor industry. According to the International Roadmap for Devices and Systems (IEEE, 2021), 2D semiconductors are being actively considered to replace Si in transistors for sub-1.5 nm node technology from 2028. Investigation of 2D metals as contact electrodes and interconnects is important because they are more compatible than bulk 3D metals in 2D circuits in terms of interface engineering (Song et al., 2020). In particular, the advent of 2D transistors with a high current density (e.g., a MoS_2 transistor with an on-state current density of 110 MA/cm^2 (McClellan et al., 2021) requires reliable metallic conductors for scalable logic applications. Ferroelectric tunnel junctions in emerging memory devices require a higher current density increase in a low-resistance state to maintain readability in massively parallel memory architectures as these devices are scaling (IEEE, 2021), which necessitates the realization of reliable, high current-carrying interconnects for crossbar arrays. SOT-driven memory devices also require a high current density for the switching of magnetization during the writing process. Despite the efforts to minimize the current density required for switching, it has been reported that a current density of 20–40 MA/cm^2 is typically required in SOT memory devices (Fukami et al., 2016; Shi et al., 2018). In addition, high-SOC $PtTe_2$ layers can be integrated with other vdW ferro- or antiferro-magnets (e.g., $CrGeTe_3$, CrI_3, and $MnPS_3$) (Chen et al., 2021; Onga et al., 2020) to develop high-performance stacked vdW spintronic nanodevices.

Limitations of the study

Evaluation using ToF-SIMS may contain unavoidable artifacts and measurement errors. For example, the depth resolution in our measurement system (~10 nm) exceeds the $PtTe_2$ film thickness, resulting in the inclusion of chemical information in the depth profile of the AlO_x substrate. Monatomic ions used for sputtering compound semiconductors can result in preferential sputtering of volatile components of the compound and changes in the chemical state and surface structure (Kubo et al., 2021; Yufit et al., 2008). Furthermore, the transport studies of $PtTe_2$ were conducted only for the 4-nm-thick polycrystalline films. The current-carrying capacity can be varied depending on its thicknesses and grain sizes. For example, the high-quality single-crystal $PtTe_2$ may exhibit even larger J_B owing to the prevention of grain boundary migration.

SUPPORTING CITATIONS

The following references appear in the supplemental information: (Cappella et al., 2013; Chen et al., 2009, 2014; English et al., 2016; Hao et al., 2018; Kang et al., 2011; Larkin et al., 2017; Lee et al., 2011; Ma et al., 2018a, 2018b; Mleczko et al., 2016; Molina-Mendoza et al., 2017; Murali et al., 2009; Neal et al., 2014; Song et al., 2019; Stolyarov et al., 2016; Taube et al., 2015; Vaziri et al., 2019; Yue et al., 2020; Zhang et al., 2015; Zhao et al., 2018).

STAR★METHODS

Detailed methods are provided in the online version of this paper and include the following:

- KEY RESOURCES TABLE
- RESOURCE AVAILABILITY
  - ○ Lead contact
  - ○ Materials availability
  - ○ Data and code availability
- EXPERIMENTAL MODEL AND SUBJECT DETAILS
- METHOD DETAILS
  - ○ Synthesis of patterned $PtTe_2$ thin films
  - ○ Structural characterization
  - ○ Device fabrication and measurements
  - ○ Extraction of decoherence length using the reduced HLN theory
  - ○ Heat dissipation model for the estimation of G_{Cox} and T_B
- QUANTIFICATION AND STATISTICAL ANALYSIS
- ADDITIONAL RESOURCES

SUPPLEMENTAL INFORMATION

Supplemental information can be found online at https://doi.org/10.1016/j.isci.2022.105346.

ACKNOWLEDGMENTS

This work was supported by the 2021 research Fund (1.210035.01) of UNIST and the National Research Foundation (NRF) of Korea (Grant Nos. 2017M3A7B8065377, 2020M3F3A2A03082444, 2021R1A2C2094674, 2021R1C1C2012306, and 2021R1A6A3A14038492) funded by the Ministry of Science, ICT, and Future Planning, and Institute for Basic Science (IBS-R019-D1).

AUTHOR CONTRIBUTIONS

S.S. prepared materials and performed most of the experiments with assistance from S.J. and J.H.; I.O. and J.-W.Y. conducted the low-temperature transport measurements; A.Y. and Z.L. conducted the (S)TEM characterizations; S.S. and S.-Y.K. wrote the article with the input of all other authors; All authors discussed the results and commented on the article; S.-Y.K. supervised the project.

DECLARATION OF INTERESTS

The authors declare no competing interests.

Received: June 8, 2022
Revised: September 26, 2022
Accepted: October 11, 2022
Published: November 18, 2022

REFERENCES

Adelmann, C., Wen, L.G., Peter, A.P., Siew, Y.K., Croes, K., Swerts, J., Popovici, M., Sankaran, K., Pourtois, G., and Van Elshocht, S. (2014). Alternative Metals for Advanced Interconnects (IEEE), pp. 173–176. https://doi.org/10.1109/IITC.2014.6831863.

Ali, M.N., Xiong, J., Flynn, S., Tao, J., Gibson, Q.D., Schoop, L.M., Liang, T., Haldolaarachchige, N., Hirschberger, M., Ong, N.P., and Cava, R.J. (2014). Large, non-saturating magnetoresistance in WTe_2. Nature *514*, 205–208. https://doi.org/10.1038/nature13763.

Altshuler, B.L., Aronov, A.G., and Khmelnitsky, D.E. (1982). Effects of electron-electron collisions with small energy transfers on quantum localisation. J. Phys. C Solid State Phys. *15*, 7367–7386. https://doi.org/10.1088/0022-3719/15/36/018.

Amit, Singh, R.K., Singh, R.K., Wadehra, N., Chakraverty, S., and Singh, Y. (2018). Type-II Dirac semimetal candidates ATe_2 (A= Pt, Pd): a de Haas-van Alphen study. Phys. Rev. Mater. *2*, 114202. https://doi.org/10.1103/PhysRevMaterials.2.114202.

Baker, M.A., Gilmore, R., Lenardi, C., and Gissler, W. (1999). XPS investigation of preferential sputtering of S from MoS_2 and determination of MoS_x stoichiometry from Mo and S peak positions. Appl. Surf. Sci. *150*, 255–262. https://doi.org/10.1016/S0169-4332(99)00253-6.

Behnam, A., Lyons, A.S., Bae, M.-H., Chow, E.K., Islam, S., Neumann, C.M., and Pop, E. (2012). Transport in nanoribbon interconnects obtained from graphene grown by chemical vapor deposition. Nano Lett. *12*, 4424–4430. https://doi.org/10.1021/nl300584r.

Cappella, A., Battaglia, J.-L., Schick, V., Kusiak, A., Lamperti, A., Wiemer, C., and Hay, B. (2013). High temperature thermal conductivity of amorphous Al_2O_3 thin films grown by low temperature ALD. Adv. Eng. Mater. *15*, 1046–1050. https://doi.org/10.1002/adem.201300132.

Chen, C.-C., Li, Z., Shi, L., and Cronin, S.B. (2014). Thermal interface conductance across a graphene/hexagonal boron nitride heterojunction. Appl. Phys. Lett. *104*, 081908. https://doi.org/10.1063/1.4866335.

Chen, G., Qi, S., Liu, J., Chen, D., Wang, J., Yan, S., Zhang, Y., Cao, S., Lu, M., Tian, S., et al. (2021). Electrically switchable van der Waals magnon valves. Nat. Commun. *12*, 6279. https://doi.org/10.1038/s41467-021-26523-1.

Chen, Z., Jang, W., Bao, W., Lau, C.N., and Dames, C. (2009). Thermal contact resistance between graphene and silicon dioxide. Appl. Phys. Lett. *95*, 161910. https://doi.org/10.1063/1.3245315.

Choudhary, N., Chung, H., Kim, J.H., Noh, C., Islam, M.A., Oh, K.H., Coffey, K., Jung, Y., and Jung, Y. (2018). Strain-driven and layer-number-dependent crossover of growth mode in van der Waals heterostructures: 2D/2D layer-by-layer horizontal epitaxy to 2D/3D vertical reorientation. Adv. Mater. Interfac. *5*, 1800382. https://doi.org/10.1002/admi.201800382.

Empante, T.A., Martinez, A., Wurch, M., Zhu, Y., Geremew, A.K., Yamaguchi, K., Isarraraz, M., Rumyantsev, S., Reed, E.J., Balandin, A.A., and Bartels, L. (2019). Low resistivity and high breakdown current density of 10 nm diameter van der Waals $TaSe_3$ nanowires by chemical vapor deposition. Nano Lett. *19*, 4355–4361. https://doi.org/10.1021/acs.nanolett.9b00958.

English, C.D., Shine, G., Dorgan, V.E., Saraswat, K.C., and Pop, E. (2016). Improved contacts to MoS_2 transistors by ultra-high vacuum metal deposition. Nano Lett. *16*, 3824–3830. https://doi.org/10.1021/acs.nanolett.6b01309.

Fukami, S., Anekawa, T., Ohkawara, A., Chaoliang, Z., and Ohno, H. (2016). A sub-ns three-terminal spin-orbit torque induced switching device. In 2016 IEEE Symposium on VLSI Technology (IEEE), pp. 1–2. https://doi.org/10.1109/VLSIT.2016.7573379.

Gall, D. (2020). The search for the most conductive metal for narrow interconnect lines. J. Appl. Phys. *127*, 050901. https://doi.org/10.1063/1.5133671.

Geremew, A., Bloodgood, M.A., Aytan, E., Woo, B.W.K., Corber, S.R., Liu, G., Bozhilov, K., Salguero, T.T., Rumyantsev, S., Rao, M.P., and Balandin, A.A. (2018). Current carrying capacity of quasi-1D $ZrTe_3$ van der Waals nanoribbons. IEEE Electron. Device Lett. *39*, 735–738. https://doi.org/10.1109/LED.2018.2820140.

Guo, S.-D., and Wang, Y. (2017). Small compressive strain-induced semiconductor–metal transition and tensile strain-enhanced thermoelectric properties in monolayer $PtTe_2$. Semicond. Sci. Technol. *32*, 055004. https://doi.org/10.1088/1361-6641/aa62bf.

Hao, S., Zeng, J., Xu, T., Cong, X., Wang, C., Wu, C., Wang, Y., Liu, X., Cao, T., Su, G., et al. (2018). Low-temperature eutectic synthesis of $PtTe_2$ with weak antilocalization and controlled layer thinning. Adv. Funct. Mater. *28*, 1803746. https://doi.org/10.1002/adfm.201803746.

Hikami, S., Larkin, A.I., and Nagaoka, Y. (1980). Spin-orbit interaction and magnetoresistance in the two dimensional random system. Prog. Theor. Phys. *63*, 707–710. https://doi.org/10.1143/ptp.63.707.

IEEE (2021). The international roadmap for devices and systems. https://irds.ieee.org/editions/2021.

Island, J.O., Steele, G.A., Zant, H.S.J.v.d., and Castellanos-Gomez, A. (2015). Environmental instability of few-layer black phosphorus. 2D Mater. *2*, 011002. https://doi.org/10.1088/2053-1583/2/1/011002.

Kang, C.G., Lee, S.K., Lee, Y.G., Hwang, H.J., Cho, C., Lim, S.K., Heo, J., Chung, H.-J., Yang, H., Seo, S., and Lee, B.H. (2011). Enhanced current drivability of CVD graphene interconnect in oxygen-deficient environment. IEEE Electron. Device Lett. *32*, 1591–1593. https://doi.org/10.1109/LED.2011.2166240.

Kim, K.-H., Hyun Jo, S., Gaba, S., and Lu, W. (2010). Nanoscale resistive memory with intrinsic diode characteristics and long endurance. Appl. Phys. Lett. *96*, 053106. https://doi.org/10.1063/1.3294625.

Kim, S.-Y., Kwak, J., Ciobanu, C.V., and Kwon, S.-Y. (2019). Recent developments in controlled vapor-phase growth of 2D group 6 transition metal dichalcogenides. Adv. Mater. *31*, 1804939. https://doi.org/10.1002/adma.201804939.

Kubo, Y., Sonohara, Y., and Uemura, S. (2021). Changes in the chemical state of metallic Cr during deposition on a polyimide substrate: full soft XPS and ToF-SIMS depth profiles. Appl. Surf. Sci. *553*, 149437. https://doi.org/10.1016/j.apsusc.2021.149437.

Larkin, L.S., Redding, M.R., Le, N.Q., and Norris, P.M. (2017). Temperature-dependent thermal boundary conductance at metal/indium-based III–V semiconductor interfaces. J. Heat Transfer *139*, 031301. https://doi.org/10.1115/1.4034938.

Lee, C.-H., Silva, E.C., Calderin, L., Nguyen, M.A.T., Hollander, M.J., Bersch, B., Mallouk, T.E., and Robinson, J.A. (2015). Tungsten Ditelluride: a layered semimetal. Sci. Rep. *5*, 10013. https://doi.org/10.1038/srep10013.

Lee, K.-J., Chandrakasan, A.P., and Kong, J. (2011). Breakdown current density of CVD-grown multilayer graphene interconnects. IEEE Electron. Device Lett. *32*, 557–559. https://doi.org/10.1109/LED.2011.2108259.

Li, J., Kolekar, S., Xin, Y., Coelho, P.M., Lasek, K., Nugera, F.A., Gutiérrez, H.R., and Batzill, M. (2021). Thermal phase control of two-dimensional Pt-chalcogenide (Se and Te) ultrathin epitaxial films and nanocrystals. Chem. Mater. *33*, 8018–8027. https://doi.org/10.1021/acs.chemmater.1c02163.

Liang, Q., Gou, J., Arramel, Zhang, Q., Zhang, Q., Zhang, W., and Wee, A.T.S. (2020). Oxygen-induced controllable p-type doping in 2D semiconductor transition metal dichalcogenides. Nano Res. *13*, 3439–3444. https://doi.org/10.1007/s12274-020-3038-8.

Liao, A., Alizadegan, R., Ong, Z.-Y., Dutta, S., Xiong, F., Hsia, K.J., and Pop, E. (2010). Thermal dissipation and variability in electrical breakdown of carbon nanotube devices. Phys. Rev. B *82*, 205406. https://doi.org/10.1103/PhysRevB.82.205406.

Liao, A.D., Wu, J.Z., Wang, X., Tahy, K., Jena, D., Dai, H., and Pop, E. (2011). Thermally limited current carrying ability of graphene nanoribbons. Phys. Rev. Lett. *106*, 256801. https://doi.org/10.1103/PhysRevLett.106.256801.

Lipatov, A., Alhabeb, M., Lukatskaya, M.R., Boson, A., Gogotsi, Y., and Sinitskii, A. (2016). Effect of synthesis on quality, electronic properties and environmental stability of individual monolayer Ti_3C_2 MXene flakes. Adv. Electron. Mater. *2*, 1600255. https://doi.org/10.1002/aelm.201600255.

Liu, H., Bao, L., Zhou, Z., Che, B., Zhang, R., Bian, C., Ma, R., Wu, L., Yang, H., Li, J., et al. (2019a). Quasi-2D transport and weak antilocalization effect in few-layered VSe_2. Nano Lett. *19*, 4551–4559. https://doi.org/10.1021/acs.nanolett.9b01412.

Liu, H., Xue, Y., Shi, J.-A., Guzman, R.A., Zhang, P., Zhou, Z., He, Y., Bian, C., Wu, L., Ma, R., et al. (2019b). Observation of the Kondo effect in multilayer single-crystalline VTe_2 nanoplates. Nano Lett. *19*, 8572–8580. https://doi.org/10.1021/acs.nanolett.9b03100.

Ma, H., Chen, P., Li, B., Li, J., Ai, R., Zhang, Z., Sun, G., Yao, K., Lin, Z., Zhao, B., et al. (2018a). Thickness-tunable synthesis of ultrathin type-II Dirac semimetal $PtTe_2$ single crystals and their thickness-dependent electronic properties. Nano Lett. *18*, 3523–3529. https://doi.org/10.1021/acs.nanolett.8b00583.

Ma, H., Dang, W., Yang, X., Li, B., Zhang, Z., Chen, P., Liu, Y., Wan, Z., Qian, Q., Luo, J., et al. (2018b). Chemical vapor deposition growth of single crystalline $CoTe_2$ nanosheets with tunable thickness and electronic properties. Chem. Mater. *30*, 8891–8896. https://doi.org/10.1021/acs.chemmater.8b04069.

Ma, R., Huan, Q., Wu, L., Yan, J., Guo, W., Zhang, Y.-Y., Wang, S., Bao, L., Liu, Y., Du, S., et al. (2017). Direct Four-Probe Measurement of Grain-Boundary Resistivity and Mobility in Millimeter-Sized Graphene. Nano Lett *17*, 5291–5296. https://doi.org/10.1021/acs.nanolett.7b01624.

Mc Manus, J.B., Horvath, D.V., Browne, M.P., Cullen, C.P., Cunningham, G., Hallam, T., Zhussupbekov, K., Mullarkey, D., Coileáin, C.Ó., Shvets, I.V., et al. (2020). Low-temperature synthesis and electrocatalytic application of large-area $PtTe_2$ thin films. Nanotechnology *31*, 375601. https://doi.org/10.1088/1361-6528/ab9973.

McClellan, C.J., Yalon, E., Smithe, K.K.H., Suryavanshi, S.V., and Pop, E. (2021). High current density in monolayer MoS_2 doped by AlO_x. ACS Nano *15*, 1587–1596. https://doi.org/10.1021/acsnano.0c09078.

Mleczko, M.J., Xu, R.L., Okabe, K., Kuo, H.-H., Fisher, I.R., Wong, H.S.P., Nishi, Y., and Pop, E. (2016). High current density and low thermal conductivity of atomically thin semimetallic WTe_2. ACS Nano *10*, 7507–7514. https://doi.org/10.1021/acsnano.6b02368.

Molina-Mendoza, A.J., Island, J.O., Paz, W.S., Clamagirand, J.M., Ares, J.R., Flores, E., Leardini, F., Sánchez, C., Agraït, N., Rubio-Bollinger, G., et al. (2017). High current density electrical breakdown of TiS_3 nanoribbon-based field-effect transistors. Adv. Funct. Mater. *27*, 1605647. https://doi.org/10.1002/adfm.201605647.

Murali, R., Yang, Y., Brenner, K., Beck, T., and Meindl, J.D. (2009). Breakdown current density of graphene nanoribbons. Appl. Phys. Lett. *94*, 243114. https://doi.org/10.1063/1.3147183.

Naylor, C.H., Parkin, W.M., Gao, Z., Kang, H., Noyan, M., Wexler, R.B., Tan, L.Z., Kim, Y., Kehayias, C.E., Streller, F., et al. (2017). Large-area synthesis of high-quality monolayer 1T′-WTe_2 flakes. 2D Mater. *4*, 021008. https://doi.org/10.1088/2053-1583/aa5921.

Neal, A.T., Du, Y., Liu, H., and Ye, P.D. (2014). Two-dimensional $TaSe_2$ metallic crystals: spin–orbit scattering length and breakdown current density. ACS Nano *8*, 9137–9142. https://doi.org/10.1021/nn5027164.

Neal, A.T., Liu, H., Gu, J., and Ye, P.D. (2013). Magneto-transport in MoS_2: phase coherence, spin–orbit scattering, and the Hall factor. ACS Nano *7*, 7077–7082. https://doi.org/10.1021/nn402377g.

Nguyen, H., Salm, C., Krabbenborg, B., Weide-Zaage, K., Bisschop, J., Mouthaan, A., and Kuper, F. (2004). Effect of thermal gradients on the electromigration life-time in power electronics. In 2004 IEEE International Reliability Physics Symposium (IEEE), pp. 619–620. http://10.1109/RELPHY.2004.1315418.

Niimi, Y., Wei, D., Idzuchi, H., Wakamura, T., Kato, T., and Otani, Y. (2013). Experimental verification of comparability between spin-orbit and spin-diffusion lengths. Phys. Rev. Lett. *110*, 016805. https://doi.org/10.1103/PhysRevLett.110.016805.

Onga, M., Sugita, Y., Ideue, T., Nakagawa, Y., Suzuki, R., Motome, Y., and Iwasa, Y. (2020). Antiferromagnet–semiconductor van der Waals heterostructures: interlayer interplay of exciton with magnetic ordering. Nano Lett. *20*, 4625–4630. https://doi.org/10.1021/acs.nanolett.0c01493.

Pace, S., Martini, L., Convertino, D., Keum, D.H., Forti, S., Pezzini, S., Fabbri, F., Mišeikis, V., and Coletti, C. (2021). Synthesis of large-scale monolayer 1T′-$MoTe_2$ and its stabilization via scalable hBN encapsulation. ACS Nano *15*, 4213–4225. https://doi.org/10.1021/acsnano.0c05936.

Pop, E. (2008). The role of electrical and thermal contact resistance for Joule breakdown of single-wall carbon nanotubes. Nanotechnology *19*, 295202. https://doi.org/10.1088/0957-4484/19/29/295202.

Rathmell, A.R., and Wiley, B.J. (2011). The synthesis and coating of long, thin copper nanowires to make flexible, transparent conducting films on plastic substrates. Adv. Mater. *23*, 4798–4803. https://doi.org/10.1002/adma.201102284.

Shi, S., Ou, Y., Aradhya, S.V., Ralph, D.C., and Buhrman, R.A. (2018). Fast low-current spin-orbit-torque switching of magnetic tunnel junctions through atomic modifications of the free-layer interfaces. Phys. Rev. Appl. *9*, 011002. https://doi.org/10.1103/PhysRevApplied.9.011002.

Sierra, J.F., Fabian, J., Kawakami, R.K., Roche, S., and Valenzuela, S.O. (2021). Van der Waals heterostructures for spintronics and opto-spintronics. Nat. Nanotechnol. *16*, 856–868. https://doi.org/10.1038/s41565-021-00936-x.

Song, S., Kim, S.-Y., Kwak, J., Jo, Y., Kim, J.H., Lee, J.H., Lee, J.-U., Kim, J.U., Yun, H.D., Sim, Y., et al. (2019). Electrically robust single-crystalline WTe_2 nanobelts for nanoscale electrical interconnects. Adv. Sci. *6*, 1801370. https://doi.org/10.1002/advs.201801370.

Song, S., Sim, Y., Kim, S.-Y., Kim, J.H., Oh, I., Na, W., Lee, D.H., Wang, J., Yan, S., Liu, Y., et al. (2020). Wafer-scale production of patterned transition metal ditelluride layers for two-dimensional metal–semiconductor contacts at the Schottky–Mott limit. Nat. Electron. *3*, 207–215. https://doi.org/10.1038/s41928-020-0396-x.

Steinhögl, W., Schindler, G., Steinlesberger, G., and Engelhardt, M. (2002). Size-dependent resistivity of metallic wires in the mesoscopic range. Phys. Rev. B *66*, 075414. https://doi.org/10.1103/PhysRevB.66.075414.

Stolyarov, M.A., Liu, G., Bloodgood, M.A., Aytan, E., Jiang, C., Samnakay, R., Salguero, T.T., Nika, D.L., Rumyantsev, S.L., Shur, M.S., et al. (2016). Breakdown current density in h-BN-capped quasi-1D $TaSe_3$ metallic nanowires: prospects of interconnect applications. Nanoscale *8*, 15774–15782. https://doi.org/10.1039/C6NR03469A.

Sung, J.H., Heo, H., Si, S., Kim, Y.H., Noh, H.R., Song, K., Kim, J., Lee, C.-S., Seo, S.-Y., Kim, D.-H., et al. (2017). Coplanar semiconductor–metal circuitry defined on few-layer $MoTe_2$ via polymorphic heteroepitaxy. Nat. Nanotechnol. *12*, 1064–1070. https://doi.org/10.1038/nnano.2017.161.

Taube, A., Judek, J., Łapińska, A., and Zdrojek, M. (2015). Temperature-dependent thermal properties of supported MoS_2 monolayers. ACS Appl. Mater. Interfac. *7*, 5061–5065. https://doi.org/10.1021/acsami.5b00690.

Vaziri, S., Yalon, E., Muñoz Rojo, M., Suryavanshi, S.V., Zhang, H., McClellan, C.J., Bailey, C.S., Smithe, K.K.H., Gabourie, A.J., Chen, V., et al. (2019). Ultrahigh thermal isolation across heterogeneously layered two-dimensional materials. Sci. Adv. *5*, eaax1325. https://doi.org/10.1126/sciadv.aax1325.

Wang, M., Ko, T.-J., Shawkat, M.S., Han, S.S., Okogbue, E., Chung, H.-S., Bae, T.-S., Sattar, S., Gil, J., Noh, C., et al. (2020). Wafer-scale growth of 2D $PtTe_2$ with layer orientation tunable high electrical conductivity and superior hydrophobicity. ACS Appl. Mater. Interfac. *12*, 10839–10851. https://doi.org/10.1021/acsami.9b21838.

Xu, H., Wei, J., Zhou, H., Feng, J., Xu, T., Du, H., He, C., Huang, Y., Zhang, J., Liu, Y., et al. (2020). High spin Hall conductivity in large-area type-II Dirac semimetal $PtTe_2$. Adv. Mater. *32*, 2000513. https://doi.org/10.1002/adma.202000513.

Ye, F., Lee, J., Hu, J., Mao, Z., Wei, J., and Feng, P.X.-L. (2016). Environmental instability and degradation of single- and few-layer WTe_2 nanosheets in ambient conditions. Small *12*, 5802–5808. https://doi.org/10.1002/smll.201601207.

Yue, X.F., Wang, Y.Y., Zhao, Y., Jiang, J., Yu, K., Liang, Y., Zhong, B., Ren, S.T., Gao, R.X., and Zou, M.Q. (2020). Measurement of interfacial thermal conductance of few-layer MoS_2 supported on different substrates using Raman spectroscopy. J. Appl. Phys. *127*, 104301. https://doi.org/10.1063/1.5128613.

Yufit, V., Golodnitsky, D., Burstein, L., Nathan, M., and Peled, E. (2008). X-ray Photoelectron Spectroscopy and Time-Of-Flight Secondary Ion Mass Spectroscopy studies of electrodeposited molybdenum oxysulfide cathodes for lithium and lithium-ion microbatteries. J. Solid State Electrochem. *12*, 273–285. https://doi.org/10.1007/s10008-007-0389-y.

Zhang, K., Wang, M., Zhou, X., Wang, Y., Shen, S., Deng, K., Peng, H., Li, J., Lai, X., Zhang, L., et al. (2021a). Growth of large scale PtTe, $PtTe_2$ and $PtSe_2$ films on a wide range of substrates. Nano Res. *14*, 1663–1667. https://doi.org/10.1007/s12274-020-2942-2.

Zhang, W., Wong, P.K.J., Jiang, S., Chen, Q., Huang, W., and Wee, A.T.S. (2021b). Integrating spin-based technologies with atomically controlled van der Waals interfaces. Mater. Today *51*, 350–364. https://doi.org/10.1016/j.mattod.2021.09.015.

Zhang, X., Sun, D., Li, Y., Lee, G.-H., Cui, X., Chenet, D., You, Y., Heinz, T.F., and Hone, J.C. (2015). Measurement of Lateral and Interfacial Thermal Conductivity of Single- and Bilayer MoS_2 and $MoSe_2$ Using Refined Optothermal Raman Technique. ACS Appl. Mater. Interfac. *7*, 25923–25929. https://doi.org/10.1021/acsami.5b08580.

Zhang, X., Woods, J.M., Cha, J.J., and Shi, X. (2020). Crossover between weak antilocalization and weak localization in few-layer WTe_2: role of electron-electron interactions. Phys. Rev. B *102*, 115161. https://doi.org/10.1103/PhysRevB.102.115161.

Zhao, B., Dang, W., Liu, Y., Li, B., Li, J., Luo, J., Zhang, Z., Wu, R., Ma, H., Sun, G., et al. (2018). Synthetic control of two-dimensional $NiTe_2$ single crystals with highly uniform thickness distributions. J. Am. Chem. Soc. *140*, 14217–14223. https://doi.org/10.1021/jacs.8b08124.

Zhou, T., and Gall, D. (2018). Resistivity scaling due to electron surface scattering in thin metal layers. Phys. Rev. B *97*, 165406. https://doi.org/10.1103/PhysRevB.97.165406.

Zhou, Y., Jang, H., Woods, J.M., Xie, Y., Kumaravadivel, P., Pan, G.A., Liu, J., Liu, Y., Cahill, D.G., and Cha, J.J. (2017). Direct synthesis of large-scale WTe_2 thin films with low thermal conductivity. Adv. Funct. Mater. *27*, 1605928. https://doi.org/10.1002/adfm.201605928.

STAR★METHODS

KEY RESOURCES TABLE

REAGENT or RESOURCE	SOURCE	IDENTIFIER
Chemicals, peptides, and recombinant proteins		
Platinum (Pt) target source	TASCO (Seoul, Republic of Korea)	CAS: 7440-06-4
Tellurium (Te) powder	TASCO (Seoul, Republic of Korea)	CAS: 13494-80-9
Software and algorithms		
OriginPro 2019	Origin Lab	https://originlab.com

RESOURCE AVAILABILITY

Lead contact

Further information and requests for resources, measurement procedures and data can be directed to the lead contact, Dr. Soon-Yong Kwon (sykwon@unist.ac.kr).

Materials availability

This study did not generate new unique reagents.

Data and code availability

Data reported in this paper will be shared by the lead contact upon request.

Any additional information required to reanalyze the data reported in this paper is available from the lead contact upon request.

EXPERIMENTAL MODEL AND SUBJECT DETAILS

This study does not use experimental methods typical in the life sciences.

METHOD DETAILS

Synthesis of patterned $PtTe_2$ thin films

The $PtTe_2$ thin films were grown using a conventional horizontal furnace system. A Pt thin film precursor (~1 nm, 99.9% purity pellet) was deposited using an e-beam evaporator (Temescal FC-2000) on dielectric substrates (e.g., SiO_2/Si or AlO_x/Si). Te powder (~0.1 g) was placed in a horizontal furnace at a distance of ~1 cm from the pre-deposited Pt thin film inside a quartz boat. Under a low pressure (0.1 Torr) at ~400°C, the evaporated Te vapor reacted with the Pt precursor, resulting in a homogenous and uniform $PtTe_2$ layer with a thickness of ~4 nm. The thickness of the as-grown thin film was controlled by modulating the thickness of the Pt precursor. To control the position, the shape of a desired pattern was defined using photolithography (MIDAS MDA-400S) with a photoresist with an undercut profile (DPRi-1549), followed by Pt deposition and lift-off. The shaped Pt precursor was tellurized using the same method as that for the thin film, resulting in the successful growth of $PtTe_2$ patterns.

Structural characterization

Micro-Raman measurements were performed using a 532 nm laser (Thermo Scientific DXR2 Raman Microscope) with a wavenumber precision of ≤ 0.066 cm^{-1}. Raman mapping (Figure S2) was performed using a Horiba LabRam HR Evolution confocal microscope with a 633 nm excitation laser. XRD patterns were obtained using a Bruker AXS D8 instrument with a Cu Kα source. AFM images were obtained using a Bruker Dimension AFM instrument in the tapping mode. XPS and ultraviolet photoelectron spectroscopy measurements were performed using an ESCALAB 250XI system (Thermo Fisher K-alpha) equipped with an Al X-ray source under ultrahigh vacuum conditions. The XPS system was calibrated by aligning the C 1s spectrum (binding energy of 284.5 eV).

High-resolution STEM images, selected area electron diffraction patterns, and EDS results were obtained using aberration-corrected FEI Titan^3 G2 60–300 with at an acceleration voltage of 200 kV. The noise in the high-resolution STEM images was subtracted using a Wiener filter. EELS was performed using a Gatan Quantum 965 dual EELS system with an energy resolution of 1.0 eV and an acceleration voltage of 200 kV. Specimens for the cross-sectional TEM analysis were prepared via an FIB (FEI Helios Nanolab 450HP) using a thick protective layer of amorphous carbon to minimize damage during the process. However, the surface damage caused by the Ga ion beam during FIB sampling was unavoidable in our experiments because an amorphous interface was observed between the protective layer and the layered $PtTe_2$ in the high-resolution STEM image (Figure S9A). As oxygen vacancy was easily induced by the Ga ion beam during the FIB sampling, the $PtTe_2$ surface had an interfacial layer of ~2 nm, with simultaneously detected signals from Te and O atoms in EELS analysis (Figure S9B).

The ToF-SIMS depth profiles were obtained using a ToF-SIMS 5 system (ION-TOF GmbH) in the dual-beam mode, with a Bi^+ ion source for collecting spectra and a Cs^+ ion source for sputtering. Considering the electronegativities of Pt and Te, the negative ion mode was selected to accurately detect oxygen ions. A pulsed 25-keV Bi^+ beam was used as the analysis source with a target current of 1.00 pA to scan crater areas of $\sim 50 \times 50\ \mu m^2$. The sputter gun was a 0.5-keV Cs^+ ion source with a target current of 39 nA, and an incident angle of 45° to the surface was used to obtain a sputtering area of $\sim 250 \times 250\ \mu m^2$.

Device fabrication and measurements

The low-temperature electrotransport and magnetotransport characterizations of the $PtTe_2$ four-probe device were conducted using Quantum Design-PPMS with a Keithley 2636A current source meter and a 2182 A nanovoltmeter at T = 3–300 K, where the carriers are injected through the wired Cu with indium dot on the $PtTe_2$ film with a Hall bar geometry (Figure S10A). The MR was measured at a constant current (I = 1 or 10 μA) depending on the applied magnetic field ($-9\ T < B < 9\ T$) at T = 3 K. Two-terminal electrical characterizations were performed using a Keithley 4200-SCS detector in a probe station (Lakeshore CRX-4K) under high vacuum ($\sim 10^{-6}$ Torr). $PtTe_2$ devices were fabricated on an AlO_x/Si substrate using a typical photolithography process and the e-beam evaporation of Pt (~40 nm) for contact electrodes. For a reasonable comparison of the $PtTe_2$ devices under air and vacuum, two groups of devices were fabricated simultaneously to ensure identical channel quality. Immediately after synthesizing the patterned $PtTe_2$ layers on the AlO_x/Si substrate with an area of $1 \times 2\ cm^2$, they were cleaved by two pieces of chips. We then simultaneously fabricated the two devices to ensure that the systematic investigation of the electrical properties was independent of the microstructure. During device preparation, the samples were maintained in a vacuum desiccator whenever possible to minimize air exposure; however, a ~15-min air exposure was necessary. After the devices were fabricated, they were stored in an UHV chamber and measured under air exposure and vacuum conditions. Annealing was not performed after the device fabrication to prevent thermal budget effect. The voltage sweep rate for the electrical field up to device failure was 10 mV s^{-1}. An electrical voltage of 0.3 V was applied every 10 s for the resistance sampling mode. The two-terminal R_c of the Pt/$PtTe_2$ interface was considered in the T_B calculations in Figure 5. For example, the electrical power (P_B) that induces Joule heating is obtained as $P_B = I_{ds}{}^2(R_{total}\text{-}2R_c) = g(T_B - T_0)L$ (See Equation 3).

Extraction of decoherence length using the reduced HLN theory

The HLN theory (in Equation 2) can reduce to the following expression;

$$\Delta\sigma(B) = \frac{\alpha e^2}{\pi h}\left[\ln\left(\frac{B_\Phi}{B}\right) - \psi\left(\frac{1}{2} + \frac{B_\varphi}{B}\right)\right] \qquad \text{(Equation 4)}$$

Figures S10E–S10G indicate that the HLN theory agrees well with the experimental data even for the reduced form in Equation 4. The calculation using Equation 4 allows extracting the phase decoherence length l_Φ ($=(h/(8\pi e B_\varphi))^{1/2}$) depending on T, which reveals the relation of $T^{-\gamma}$ (Figure S10G). We found that the value of γ is $\sim 0.39 \pm 0.06$, implying the electron dephasing could be attributed to electron-electron interactions (γ = 0.5) compared to electron-phonon interactions (γ = 1). This conclusion concurred with that deduced from Equation 2.

Heat dissipation model for the estimation of G_{Cox} and T_B

In heat dissipation model in Equation 3, g is the parallel combination of spreading thermal resistance in the Al_2O_3 (R_{ox}), the thermal resistance from oxide to Si (R_{si}), and thermal contact resistance at the $PtTe_2$/oxide interface (R_{Cox}) as follows (Behnam et al., 2012; Liao et al., 2011);

$$\frac{1}{g} = \frac{R_{Cox} + R_{ox} + R_{si}}{W} = \frac{R_{Cox}}{W} + \left\{ \frac{\pi k_{ox}}{\ln\left[6\left(\frac{t_{ox}}{W} + 1\right)\right]} + \frac{k_{ox}}{t_{ox}} W \right\}^{-1} + \frac{1}{2k_{si}} \left(\frac{L}{W_{eff}} \right)^{\frac{1}{2}} \qquad \text{(Equation 5)}$$

Here, t_{ox} is the thickness of Al_2O_3, $W_{eff} \approx W + 2t_{ox}$ is the effective width of the heated region at the Al_2O_3/Si interface by the fringing effect (Behnam et al., 2012), k_{ox} is the thermal conductivity of Al_2O_3 (~1.5–2.0 $Wm^{-1}K^{-1}$ depending on the temperature of the oxide, $T_{ox} \approx (T_B + T_0)/2$) (Cappella et al., 2013), and $k_{si} \approx 24{,}000/T_0$ is the Si thermal conductivity, where T_0 is the ambient temperature of the measurement. In a simplified form, the g is affected by the dimensions of a device channel (i.e., $g \propto (W/L)^{1/2}$). Because the channel is 'long' enough to transport most of the heat vertically rather than laterally, the heat dissipation model utilized in this study (Equation 3) does not account for thermal contact resistance (R_T) at the channel-metal contact interface. To be specific, heat conduction with a finite R_T is expressed (Behnam et al., 2012; Pop, 2008) as;

$$P_B = g(T_B - T_0)L \times \frac{\cos h\left(\frac{L}{2L_H}\right) + gL_H R_T \sin h\left(\frac{L}{2L_H}\right)}{\cos h\left(\frac{L}{2L_H}\right) + gL_H R_T \sin h\left(\frac{L}{2L_H}\right) - 1} \qquad \text{(Equation 6)}$$

Here, $L_H = (k_{channel}/g)^{1/2}$ denotes the thermal healing length along the channel and $R_T = [L_{Hm}/(k_m t_m (W+2L_{Hm}))]$, where $k_{channel}$ is the lateral thermal conductivity of $PtTe_2$ and L_{Hm} ($= (k_m t_{ox} t_m / k_{ox})^{1/2}$) is the thermal healing length of heat propagating into the metal contacts, k_m is thermal conductivity of metal contact (i.e., Pt), and t_m is thickness of contact. If the L is much longer than L_H, Equation 6 reduces to $P_B = g(T_B - T_0)L$ (by considering $sinh(x) = cosh(x) = exp(x)/2$ for $x >> 1$), which is equivalent to Equation 3. Therefore, for a long device ($L >> L_H$), it is permissible to ignore the impact of R_T on heat conduction ($R_T \approx 0$), as most of the heat sinks vertically through the underlying Al_2O_3. In our $PtTe_2$ devices, the L_H can be in the range of 73–140 nm on average at RT, considering our $k_{channel}$ (~2.2 W $m^{-1}K^{-2}$ calculated by the Wiedemann-Franz law for our $PtTe_2$ thin film (Figure S14C), whereas the simulated value approaches ~7.9 W $m^{-1}K^{-2}$ (Guo and Wang, 2017)). Since the L for our measured devices was ~1.5–10 μm, which is more than ten times longer than the L_H, the simplified version of the heat dissipation model (Equation 3) is applicable.

QUANTIFICATION AND STATISTICAL ANALYSIS

Figures represented averaged or representative results of multiple independent experiments. Analyses and plots were performed with Origin.

ADDITIONAL RESOURCES

There are no additional resources needed to be declared in this manuscript, additional requests for this can be made by contacting the lead contact.